Contents lists available at ScienceDirect

Comptes Rendus Physique

www.sciencedirect.com

Physics and arts / Physique et arts

Joint data treatment for Vis–NIR reflectance imaging spectroscopy and XRF imaging acquired in the Theban Necropolis in Egypt by data fusion and t-SNE

Traitement conjoint par fusion de données et T-SNE des données acquises par imagerie de spectroscopie de réflectance Vis–NIR et par imagerie XRF dans la nécropole thébaine (Égypte)

Matthias Alfeld [a],[*], Silvia Pedetti [a], Philippe Martinez [a],[b], Philippe Walter [a]

[a] *Sorbonne Université, CNRS, Laboratoire d'archéologie moléculaire et structurale, LAMS, 75005 Paris, France*
[b] *Mission archéologique française de Thèbes-ouest (MAFTO), Centre d'étude et de documentation sur l'Ancienne Égypte (CEDAE), Ministry of Antiquities, 3 El-adel Abu Bakr St. Zamalek, Cairo, Egypt*

A R T I C L E   I N F O

A B S T R A C T

Hyperspectral imaging allows the acquisition of representative information on cultural heritage objects. For a complete identification of the chemical compounds present, one needs instruments employing different forms of radiation, sensitive to different chemical features. Data treatment workflows are commonly developed for a single spectroscopic technique, so that data sets are evaluated separately, and the reduced representations yielded are compared during interpretation. In this publication, we describe how t-stochastic neighbor embedding (t-SNE) allows for the evaluation and interpretation of data acquired in a Ramesside tomb (13th century BC) of the Theban Necropolis in Egypt. By fusing X-ray Fluorescence (XRF) imaging and Reflectance Imaging Spectroscopy (RIS) into a single data set, we exploit the synergies between both methods to support interpretation and presentation of the results yielded.

© 2018 Académie des sciences. Published by Elsevier Masson SAS. This is an open access article under the CC BY-NC-ND license (http://creativecommons.org/licenses/by-nc-nd/4.0/).

R É S U M É

L'imagerie hyperspectrale permet l'acquisition d'informations représentatives sur les objets du patrimoine culturel. Pour une identification complète des composés chimiques présents, il faut des instruments employant différentes formes de rayonnement, sensibles à différentes caractéristiques chimiques. Les procédures pour évaluer les données sont généralement développées pour une seule technique spectroscopique. Les données issues de différentes techniques sont donc évaluées séparément et les représentations obtenues par des données réduites sont comparées pendant l'interprétation. Dans cette publication, nous décrivons comment la méthode « t-stochastic neighbor embedding » (t-SNE) permet l'évaluation et l'interprétation des données acquises dans une tombe ramesside (XIIIᵉ siècle

---

* Corresponding author.
  E-mail address: matthias.alfeld@gmx.de (M. Alfeld).

avant J.-C.) de la nécropole thébaine en Égypte. En fusionnant l'imagerie par fluorescence X (XRF) et la spectroscopie d'imagerie par réflectance (RIS) en un seul ensemble de données, nous exploitons les synergies entre les deux méthodes pour étayer l'interprétation et la présentation des résultats obtenus.

1. Introduction

The process of an artwork's creation is an integral part of its core identity. It reflects the training of the artist, but also the price, hue, mechanical properties and the perceived value of the materials available, especially pigments. Consequently, the "materiality" of an object (*e.g.*, its chemical composition) is an integral part of cultural heritage as it not only contains clues to the cultural practices followed in its production, but also is an expression of this heritage itself.

As visual inspection provides only limited insight into the chemical composition of an object, scientific methods are needed for the study of cultural heritage artefacts. In recent years, spectroscopic spot investigations have been more and more complemented, and partly replaced by hyperspectral imaging methods, especially for historical paintings, but also for other objects. These methods do not only allow one to acquire representative information on heterogeneous objects, but also to visualize the distribution of compounds and so to gain insight into sub-surface paint layers and the sequence of painting [1]. The most mature and popular techniques are X-Ray Fluorescence (XRF) imaging and Reflectance Imaging Spectroscopy (RIS) in the visible and near infrared (IR) [2].

XRF probes the inner shell electrons of an element whose energy is largely independent of its chemical state and thus provides clear and easily interpretable elemental information. In the wavelength range commonly employed by RIS (400–2500 nm), transitions in the outer shell electron levels are probed, as are vibrational transitions (overtones and combination bands) [3]. Both techniques are hyperspectral techniques, as for each pixel a continuous spectrum is recorded.

For both techniques, mature instruments are commercially available. But how much information can be obtained by them is not only dependent on their technical capabilities, but also on data treatment, which is structured in four phases:

- *exploration*: all relevant chemical features in the data set are identified;
- *evaluation*: the hyperspectral data is reduced to a *representation* (a set of distribution images and spectra) that contains all relevant chemical features in a legible manner;
- *interpretation*: conclusions are drawn based on the *representation*, ultimately aiming at answering the research question;
- *presentation*: the conclusions drawn are communicated to collaborators and the scientific community with parts of the *representation* as arguments.

Ultimately, *presentation* is the goal of any scientific study, but commonly only a small part of the data recorded is used in this last phase. This last phase is furthermore done in general with a delay after data-gathering, thus for the routines used here, the processing time is not critical.

Exploration/evaluation/interpretation, however, are time critical, as one needs to assure the quality of data after acquisition and draw (preliminary) conclusions to decide on the next measurements. And each of these phases has to be considered important as its results are used in the next one.

For individual data sets of a single spectroscopic technique, workflows have been established for all phases of data treatment. When multiple data sets, originating from different samples and/or techniques, are available, *exploration/evaluation* is commonly done separately, with the *interpretation* being done by using a set of reduced *representations*, *e.g.*, [3]. This also means that possible synergies between different methods are only exploited late in the data treatment.

Fusing the data, *i.e.* combining different data sets into a single one, is seldomly done. It is easy to fuse data horizontally, *i.e.* to combine data of the same technique to obtain a single representation for several data sets [4]. A vertical fusion of data, *i.e.* the stacking of the different data sets obtained by different techniques on the same object, is seldomly attempted as it requires an alignment of the hyperspectral data cubes and no established data treatment procedures yet exist. However, it has been described before for cultural heritage objects, e.g., to enhance the apparent resolution of coarse elemental distribution images acquired by XRF using better resolved RIS data [5]. But also, in this case, the synergy between the methods is not truly used during the *evaluation*.

In this paper, we present a novel approach to the joint *evaluation* of XRF and RIS data by vertical data fusion and t-distributed stochastic neighbor embedding (t-SNE). t-SNE projects high-dimensional hyperspectral data into an easily legible two-dimensional *representation* and was introduced to RIS only recently [6].

We demonstrate this approach on data acquired in the Theban Necropolis in Egypt from the tomb of Nakhtamun (TT341), "chief of the altars in the Ramesseum" [7], the Ramesseum being the memorial temple of Ramses II (19th dynasty, 13th century B.C.). Nakhtamun's tomb chapel is thus commonly believed to have been decorated during his reign. Most of the tomb's decorated surfaces were investigated by RIS and areas of special interest were investigated by XRF. We selected for this paper a scene showing the deceased on his way to the afterlife facing three goods. This small area was investigated
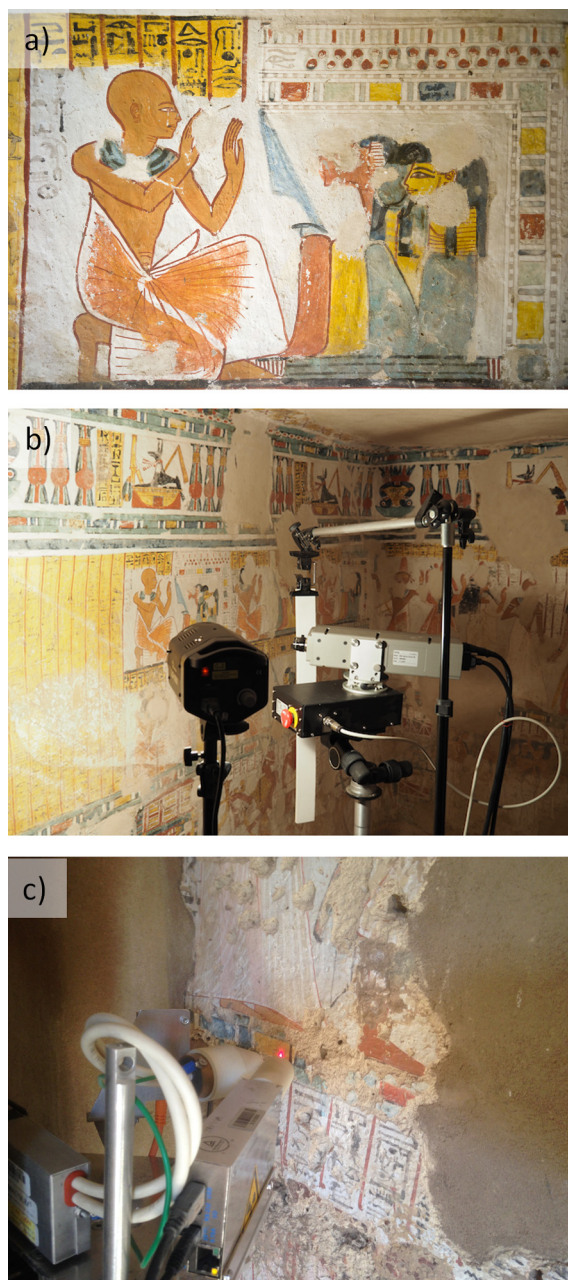
Fig. 1. a) Investigated area in the tomb of Nakhtamun (TT341), showing the deceased (left) negotiating with three gods for his passage into the netherworld. b) RIS instrument during the investigation of the area. c) XRF measurement head at work on site.

by both techniques (see Fig. 1a). It can be seen that several parts of the painting were lost over the millennia, but these holes were filled with a white material during conservation treatment done in recent years. The goal of our investigations was the identification of pigments and painting techniques during the reign of Ramses II and the 19th dynasty. Albeit some questions remain open, the use of pigments in ancient Egypt is comparably well documented [8], but only few publications detail the painting technique of this period of ancient Egypt.

In what follows we will describe the instruments used and the experimental conditions. This will be followed by a discussion of established and fused data *exploration/evaluation* approaches and an *interpretation* of the *representations*.

2. Experimental

The RIS data was acquired with a commercial VNIR Spectral Camera HS V10E built by Specim (Oulu, Finland) sensitive to the spectral range from 400 to 1000 nm, which recorded the light of a 1-kW halogen lamp reflected by the wall. For the
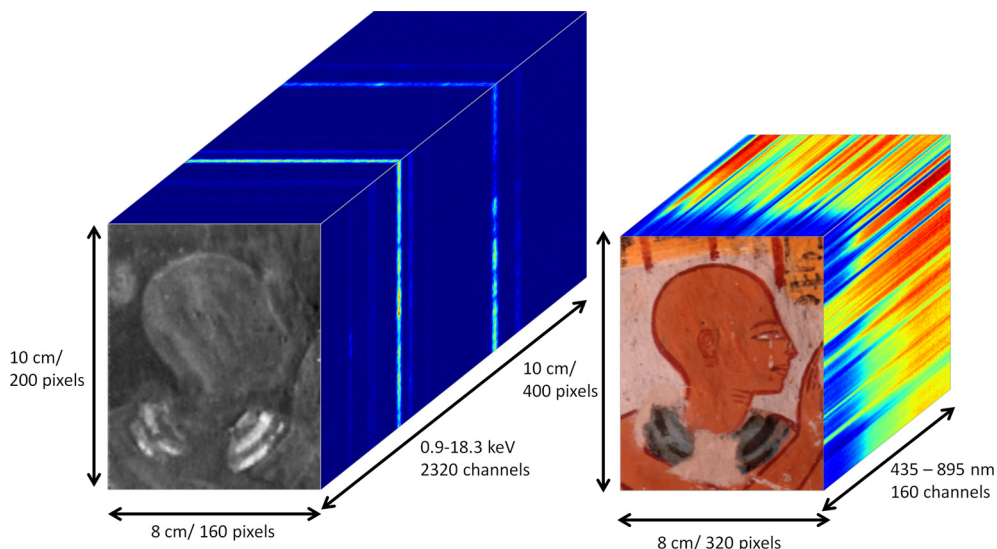
Fig. 2. Hyperspectral data cubes acquired by XRF and RIS.

measurement on site, the camera was mounted on a motorized rotation stage. The acquired RIS data were normalized with respect to an external Spectralon white reference (Specim). This accurately compensated for variation of the illumination spectrum and the spectral response of camera in the central spectral range (435–895 nm).

The XRF scanner was built in-house using a 3-W Pd transmission anode X-ray tube, a Si-drift detector (SDD), and a laser distance measurement device for positioning. For the acquisition of data, source and detector were moved in parallel to the surface by two motorized stages of 30 cm travel range, scanning the wall with a primary beam 1.0 to 1.2 mm in diameter. The instruments are shown in Fig. 1b and c, their hyperspectral data cubes in Fig. 2.

On site, the measurement heads were mounted on photography tripods to position them in front of the investigated areas. Both instruments were described in detail elsewhere [9].

While both instruments acquire hyperspectral data cubes, their mode of acquisition differs. With the XRF scanner, each point of the image is exposed to X-rays in a sequential manner and the image is acquired pixel by pixel (*whisk-broom* scanning). The image was acquired with a pixel size of 0.5×1.0 mm ($h \times v$) and a dwell time of 200 ms/pixel in 106 minutes. Given the size of the primary beam ($\sim$1.1 mm), the data was horizontally oversampled. After acquisition, the data was interpolated to a uniform pixel size of 0.5×0.5 mm, yielding an apparent higher lateral resolution, due to oversampling.

The RIS scanner is a *push-broom* or line scanner, i.e. it is acquiring one vertical line of the image and, by rotating it in the horizontal plane, the image is acquired line by line. This is realized by projecting the image seen by the camera on a slit, thus selecting a line in the image, and guiding this on a dispersive optic. The radiation dispersed by this element is projected on a CCD, which is recording in one-dimension spectral information and in the other lateral information. Each line was acquired for 220 ms, yielding under the chosen experimental conditions a pixel size of 0.25 mm. Consequently, the RIS data of the area in question was acquired in 40 s. Reference spectra were prepared from pigments obtained from various manufacturers using the same RIS instrument. For this approach, the pigments were applied with limewater and animal glue binders on marble plates.

Details on the instruments and the preparation of reference samples are given in the Digital Support Information (DSI).

3. Data treatment

In Fig. 2, the hyperspectral data cubes of XRF and RIS are shown. Whereas the XRF data shows sharp bands (fluorescence lines), the RIS features are more broadly and less specific. Consequently, the established procedures for *exploration* and *evaluation* phases vary considerably.

XRF data is *explored* by inspecting the sum and maximum pixel spectra of the data set that are shown in Fig. 3. The sum of all spectra in the data cube allows identifying most elements present by the known energy of their fluorescence lines. The maximum pixel spectrum shows the highest intensity that any energy channel reaches in the entire hypercube and allows the identification of elements that are present only locally.

The underlying physics are well understood and consequently the profile of fluorescence lines can be calculated and each spectrum in the hypercube is expressed as a linear combination of these profiles and a term for the spectral continuum below them. The final *representation* yielded corresponds to a series of qualitative elemental distribution images in that the brightness corresponds to the intensity of the recorded fluorescence line (Fig. 3). Thus, XRF allows one to conclude with regard to the pigments used. It allows in principle for a quantification of the elements present, but this requires good
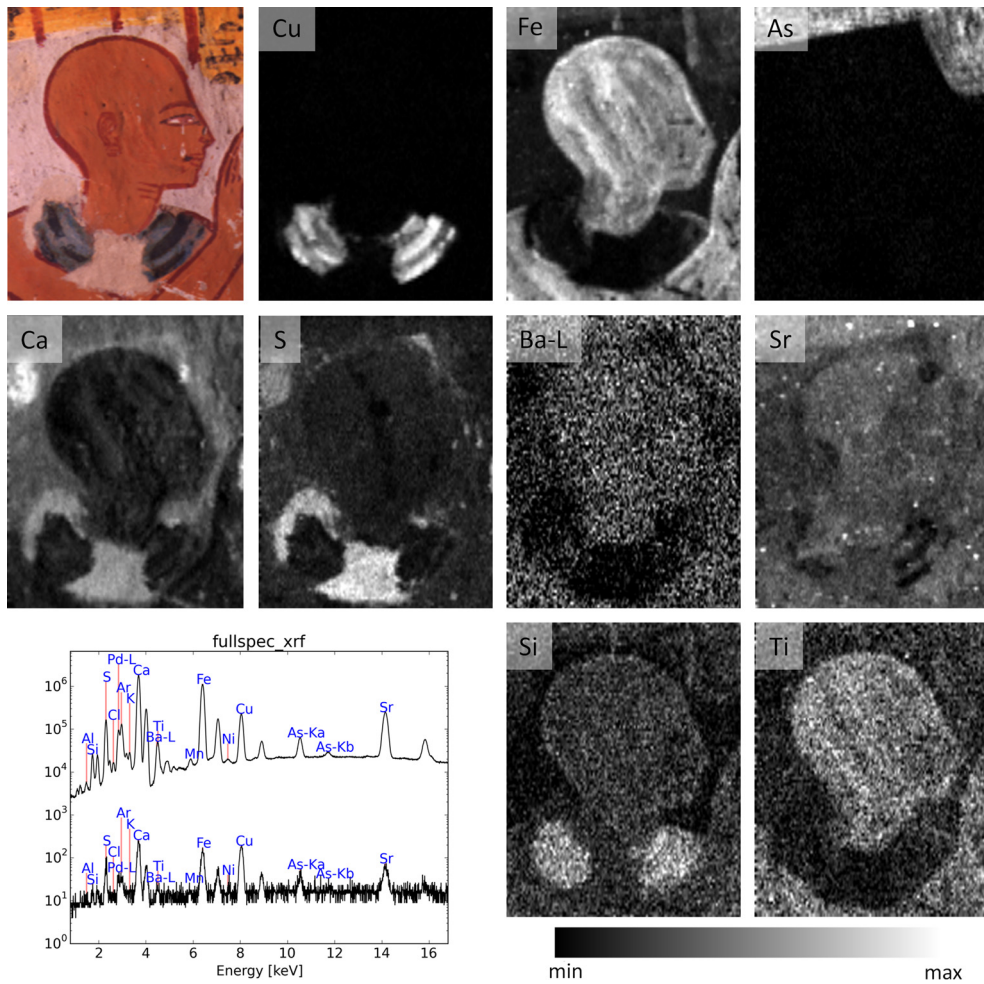
Fig. 3. Elemental distribution images acquired by XRF. The plot shows sum and maximum pixel spectra.

statistics and a good knowledge of layer thickness and composition that is not accessible in this case. These operations were performed, using the *PyMCA* [10] and *datamuncher* [11] software packages, the latter publication describing also advanced *exploration* and *evaluation* possibilities.

RIS data is *explored* by searching *endmembers*. These are "pure" spectra that cannot be expressed as a non-negative linear combination of the other spectra in the hypercube. The *endmembers* are manually selected from a *representation* of the data by few principal components, determined by minimum noise fraction transformation (MNF). Use was made of the ENVI software package (Harris Corporation, Melbourne, Florida, USA). By comparing these *endmembers* to reference spectra, the pigments present can be identified.

As the calculation of reflectance spectra is less straightforward than for XRF spectra, the *evaluation* of RIS data is commonly done by Spectral Angle Mapping (SAM), which applies hard clustering of each spectrum/pixel to the nearest *endmember*. As a measure for distance, the spectral angle (or cosine distance) is used, which is the angle between two spectra if they are understood as high-dimensional vectors. If the distance to any *endmember* is larger than a user defined threshold, the spectrum/pixel is unassigned. The yielded *representation* features binary images and the spectra of the *endmembers* (Fig. 4). The data treatment for RIS data has been summarized elsewhere [12].

To fuse XRF and RIS data, a correct alignment was necessary. For this, common features were searched for by SIFT (Scale-Invariant Feature Transform) in monochromatic *representations* of both data sets. For RIS, the visible spectral range was integrated, and the resulting image was smoothed to have the same apparent lateral resolution as the XRF data. The XRF representation was calculated by subtracting Fe and Cu distribution images from the Ca one and normalizing it. Both images and the features found are shown in Fig. 5d.

To fuse the two hyperspectral data cubes, meaningful spectral ranges free of artefacts were selected in both (435–895 nm for RIS and 0.9 to 18.3 keV for XRF). In addition to the normal RIS data, the first derivative of the reflectance data was added. We observed that this allowed for a better separation of the red and skin tones as this put more statistical weight

on the precise position of the edge in the reflectance data. The resulting fused data cube had 32,000 pixels (160×200) with 784 channels.

t-SNE aims at yielding a two-dimensional *representation* of the data in that the *probability* that one spectrum/pixel chooses another as a neighbor is identical to that in the original, high-dimensional data, based on the Euclidean distance. If one would try to project these distances directly into two dimensions, one would yield an illegible cloud of points. But by plotting probabilities and using, in the high-dimensional, case Gaussian statistics and, in the two-dimensional case, the steeper Student statistics, it is possible to yield in an iterative process a clearly legible *representation*. When, in a t-SNE *representation*, two pixels are close, this is indicating a high degree of similarity, but a large distance between them does not quantify the dissimilarity [13]. Ten t-SNE *representations* were calculated with identical parameters in 2000 s each on a 2015 Macbook Pro with the t-SNE module of scikit-learn (scikit-learn.org, version 0.19.1). While not identical, all provided the same information. One t-SNE *representation* is shown in Fig. 6, the clusters manually selected in it, and the mean spectra of these clusters are shown in Fig. 7.

Details on the data treatment for RIS, the alignment of the data sets, and t-SNE are given in the DSI.

4. Results and discussion

4.1. XRF imaging

In Fig. 3, elemental distribution images *representing* the acquired XRF data are shown. As the color scale is defined by the most and least intense pixel, a dark pixel does not indicate the absence of an element if it is present throughout the investigated area. Given the penetrative nature of X-rays, signals from surface layers as well as below them are recorded.

In the top-most row, the elements related to the main pigments are shown. Cu is present in the pigment Egyptian blue (**CaCuSi**$_4$O$_{10}$, **bold elements** are detectable by our XRF instrument) used in Nakhtamun's collar. The varying thickness of the paint layer is clearly visible in this image. Another Cu-containing pigment is Egyptian green. Its synthesis was similar to that of Egyptian blue but with an excess of silicate, yielding different compositions and shades (**CaCuSi**$_4$O$_{10}$ + **Si**O$_2$). Fe is present in a red pigment, probably hematite (**Fe**$_2$O$_3$), used in the red outlines. It can be assumed to be present also in the skin tone, albeit mixed with another pigment, probably also Fe based. Here goethite (α-**Fe**O(OH)) is more likely than jarosite (**KFe**$_3$(OH)$_6$(**S**O$_4$)$_2$), as no significant K signals were recorded. As, finally, is present in the yellow orpiment (**As**$_2$**S**$_3$) or the red–orange realgar (**As**$_4$**S**$_4$)[8].

In the second and third rows, minor components and weakly detected elements are shown. Si is present in Egyptian blue, but is seems to be also a minor component in the Fe-containing pigments. Ti seems to be correlated with the skin tone, probably due to the presence of ilmenite (**FeTi**O$_3$), which has been reported previously to be present with goethite in ancient Egypt paint ([14], cited after [15]). Sr is present throughout the area, which is unsurprising as it often is present in the same components as Ca and can be detected from deeper depth as its signals are less absorbed in covering layers, due to the higher energy of its characteristic radiation (Ca Kα: 3.69 keV, Sr Kα: 14.1 keV).

Ba seems to be present throughout the investigated area with varying abundance. Notably, it is absent in the restored areas that are clearly visible in the Ca and S images. Ca is present in all known white pigments used by the ancient Egyptians (calcite **Ca**CO$_3$, gypsum, **Ca**S O$_4$·2H$_2$O, anhydrite **Ca**S O$_4$, huntite Mg$_3$**Ca**(CO$_3$)$_4$) [8]. However, the S distribution shows that gypsum was used in the repairs, but not in the other white areas. The low abundance of S in the original white areas suggests the use of calcite, but given the limits of the methods used, the use of huntite cannot be excluded.

4.2. Reflectance imaging spectroscopy

In Fig. 4, the *representation* of the RIS data obtained by SAM is shown. Given the employed wavelength, only the surface layers contribute to the recorded spectra. The *endmember* 1 shows the dark red outline of the painted area. Its reflectance spectrum is similar, within the limits of the data, to a reference spectrum of red ochre/hematite and thus, together with the XRF data, confirms its identity. The beige/pink skin color represented by *endmember* 2 can be well expressed as a mixture of red and yellow ochre (hematite and goethite respectively) reference spectra, making use of the Kubelka–Munk equation [16]. The *endmember* 3 represents the white area, original and restored. In the absence of characteristic features, the spectrum of the chalk reference does not contradict the identification as calcite or gypsum. The fourth endmember describing the yellow area cannot be described either by yellow ochre or by orpiment, but by a mixture of both. As we can observe in the endmember spectrum the characteristic reflectance feature of goethite at 450 nm, we can conclude that here a mixture of goethite and orpiment was used. Finally, the blue collar is represented by the *endmembers* 5–7. The *endmembers* 5 and 6 represent thicker and thinner layers of Egyptian blue. The reference spectrum shows three clearly distinct maxima at 445, 720, and 915 nm. Only the IR luminescence band around 725 nm is clearly discernible in the *endmembers*. However, the presence of Cu and Si and IR luminescence allows a definite identification of Egyptian blue. From the area of *endmember* 6 in a later scan with higher lateral resolution spectra were selected that showed great similarity to the reference spectrum. *endmember* 7 shows no IR luminescence; only a broad reflection maximum around 545 nm is observed. The Egyptian green reference spectrum that we acquired had a reflectance maximum around 498 nm, but it is known that the observed color of Egyptian green varies [8]. We assume that this is indeed preserved Egyptian green and that the collar was shaped from altering bands of blue and green. While the better part of the green was lost, the thick layers of Egyptian blue are better
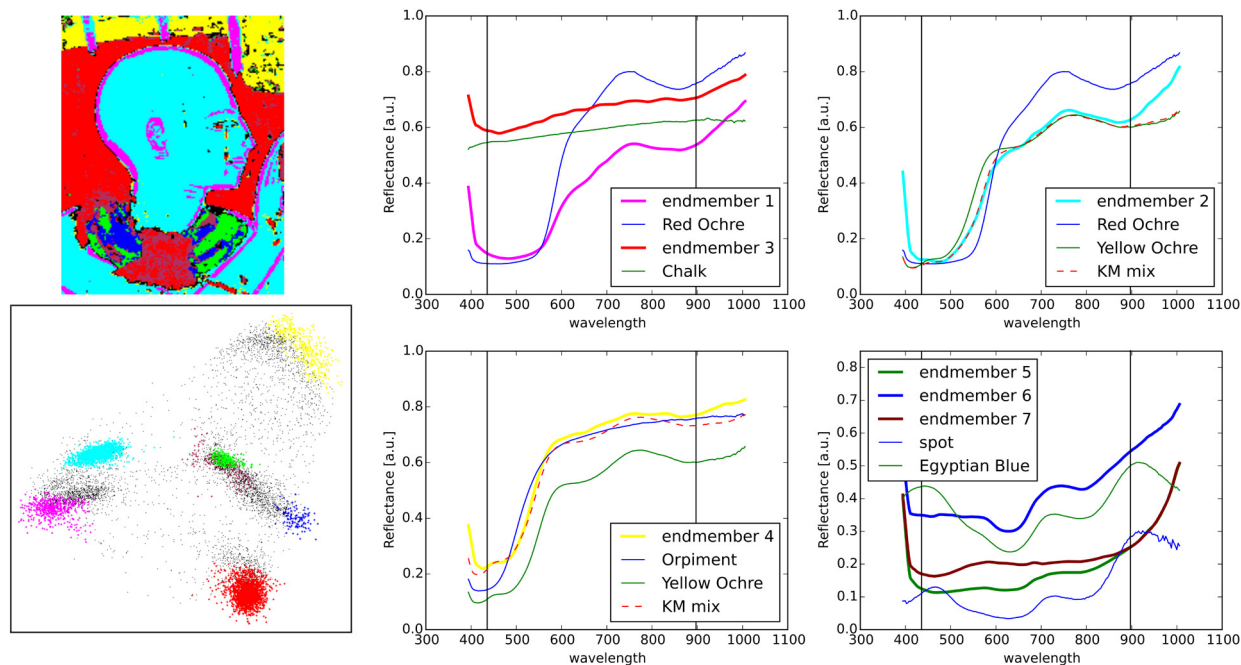
Fig. 4. SAM results of RIS data. In the left column, the distribution of clusters is shown, as is a plot of the first three principal components with highlighted *endmembers*. The plots show *endmembers* and reference compounds. The spectrum indicated "spot" was selected from a later scan with higher resolution of the area of endmember 6. "KM mix" indicates virtual mixing of pigments using the Kubelka–Munk equation. The vertical black lines indicate the spectral range taken into account during data treatment and KM mixing.

preserved. The fact that we detect throughout the area Egyptian blue and observed a slight blue tone suggests that the final layers of Egyptian green and blue were applied on a homogeneous, thin layer of Egyptian blue.

RIS with SAM provides a good overview of pigment use, but the yielded *representation* is imperfect. Some pixels in the white background are part of the cluster of *endmember* 7 as the cosine distance between featureless white reflectance and the weak features of Egyptian green is small, while the difference in absolute reflectance is rather high.

Some pixels present mixed spectra from different pigments for reasons other than the application of pigment mixtures. One reason is the partial transparency of layers. The other is that, on the border between colored areas, the limited lateral resolution of the camera results in a combination of the characteristic spectra being recorded for this pixel. Both effects can be mainly seen in the pixels attributed to endmember 2. In the upper left corner, the dark red lines on the yellow background are partly transparent and attributed to this cluster. Further, the border between dark red and white paint is often attributed to endmember 2, albeit the skin color is not discernible here in visual inspection, even with high magnification.

4.3. Data fusion and t-SNE

In Fig. 5d, the features detected for aligning the XRF and RIS data are shown. Next to data fusion, it allows one to transfer the visible outline of the painting to the XRF *representation* (Fig. 5a–c). This highlights the fact that, in some areas, elemental distribution and visual impression are not in agreement. The Fe distribution extends notably out of the visible contour to the right of the mouth (Fig. 5b). These covered paint layers are in fact visible in some areas by visual inspection. A high-resolution photograph shows that the white paint was applied not only on the skin color but also on the red outline (Fig. 5e). Such visual inspections provide precious local information but no representative one, unlike XRF imaging. The As distribution (Fig. 5c) highlights that the yellow background of the hieroglyphic text was originally larger and later reduced by the application of white paint.

The painting technique for the 18th dynasty (16th–14th centuries B.C.) has been described in detail [17]. While observations from this earlier period are not necessarily directly transferable, some parallels can be observed: after filling areas predefined by a preliminary sketch with colors, the painter applied the final contour lines with red paint. Afterwards, the color exceeding these contours was covered up by the application of white paint of a hue close to the background. This is in good agreement with the observations in this data.

The results of evaluating the fused data by t-SNE are shown in Fig. 6. The indicated clusters were manually selected, first according to their apparent distribution and color. In a second step, they were refined by inspecting the distribution of the clusters in the visible image, the average spectra of the clusters and *a priori* knowledge.
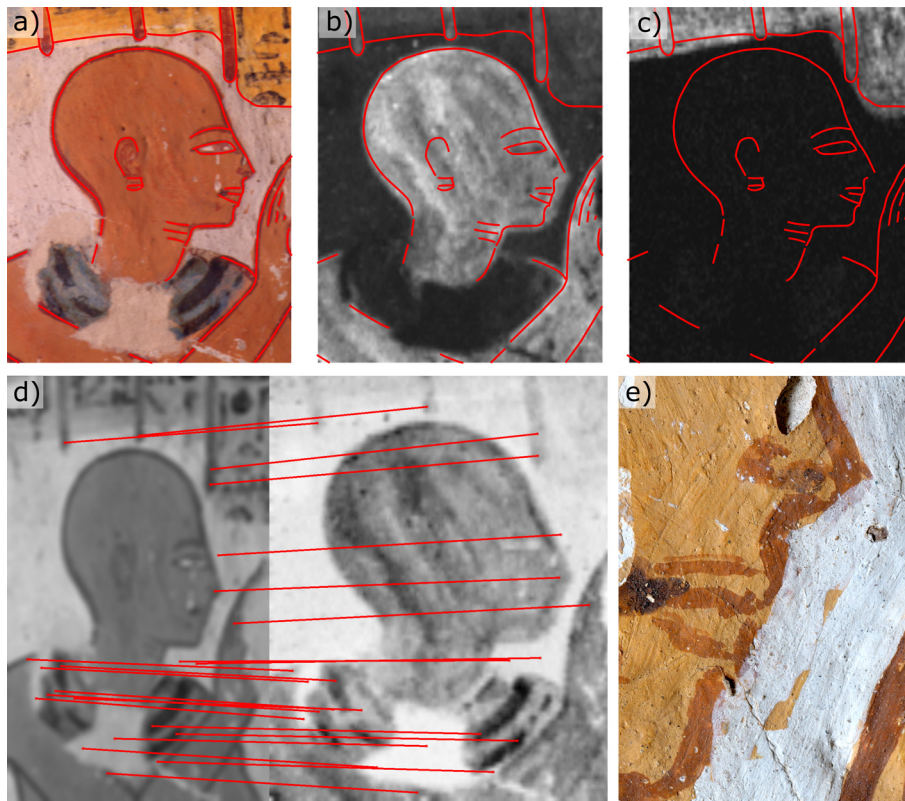
Fig. 5. Image alignment. Upper row: visible image with contour lines (a), Fe (b), and As (c) distribution images with transferred contour lines. Bottom row: common features found in RIS data and XRF data by SIFT (d). e) macro photograph of the deceased's nose and lips.
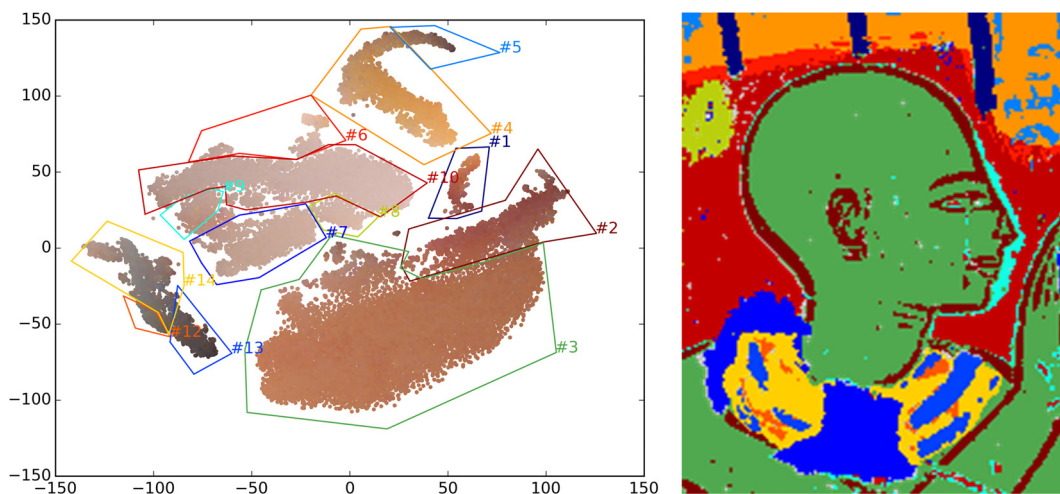

Fig. 6. Left: scatter plot of t-SNE representation with each symbol having the same color as the pixel in the RGB data. Right: clusters in the investigated area. The color of the clusters is identical in both parts of the figure.

Meaningful clusters are shown in Fig. 7. For each cluster, the distribution is shown and, in the same color, the associated mean reflectance spectra, their first derivatives, and the XRF spectra. In the first derivatives of all spectra, an artifact is visible at 693 nm.

The first group of clusters, describing Fe-based pigments, is shown in Fig. 7a. Clusters 1 and 2 are very similar in terms of reflectance spectrum, but they are shown to be distinct by the strong As signal of cluster 1. This is due to the fact that both represent hematite-based paint, but cluster 1 was applied on a yellow area, while cluster 2 was applied on the skin color. As RIS is only surface sensitive and XRF also probes the sub surface layers, the orpiment layer does not contribute to the reflectance spectrum.
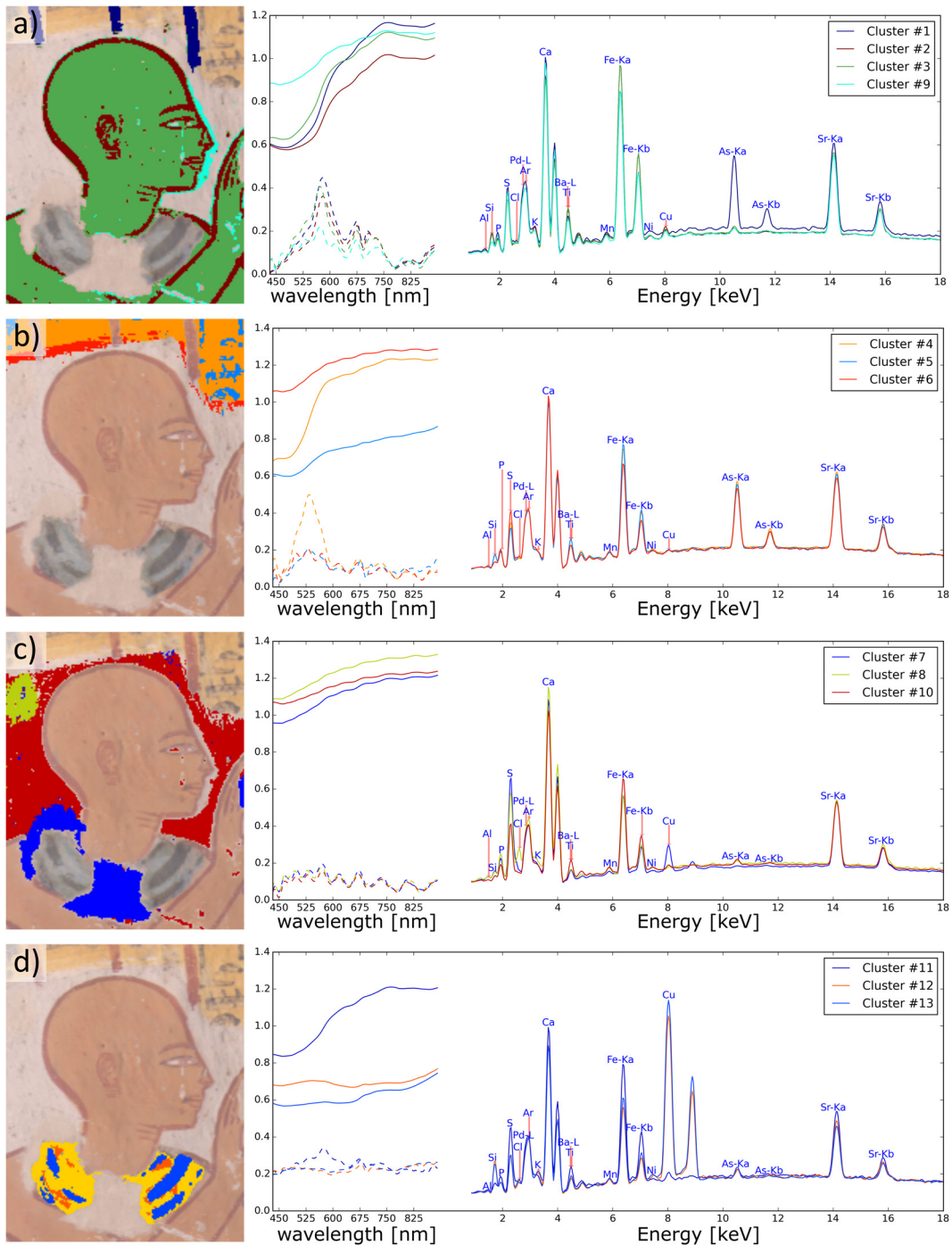
Fig. 7. Selected clusters from the t-SNE representation as distribution images and mean spectra. The first derivative of the reflectance data was placed below it for ease of comparison. The *Y*-axis is in arbitrary units.

Cluster 3 corresponds to the skin tone. It is very similar to cluster 2 in terms of XRF spectrum, which is not surprising as the latter represents only a thin layer that does not strongly absorb radiation emitted by lower layers. Cluster 2's Ti–K signal (4.95 keV), however, is stronger than that of cluster 1, which represents the hematite-based paint used for the outlines more purely. Consequently, we can consider Ti as a characteristic trace for the pigment mixture used for the skin tones, possibly in the form of ilmenite, as discussed above. This can also be concluded from the elemental distribution image of Ti (Fig. 3), but it is difficult to confirm there. All three clusters feature a Si signal, a typical impurity for earth pigments.

Cluster 9 mainly represents the overpainted part of the skin tone discussed above, so that, while featuring a strong Fe signal, it is, in terms of reflectance spectrum, similar to the white paint. The cluster has also several pixels in the border between red and white paint due to the limits of lateral resolution discussed above.

The clusters in Fig. 7b are similar in terms of XRF data. Cluster 4 describes the orpiment-containing yellow reserve, cluster 5 the dark ink that was used to draw the hieroglyphs. The fact that cluster 5 does not feature an enhanced P signal confirms that it was not obtained by the burning of bones, as expected. The reasons for the enhanced Si signal are unknown, but may be linked to the addition of clay to the ink or the fact that the dust sticks better to the black ink than to the yellow area. Cluster 6 describes part of the yellow paint that was overpainted with white in a final step. Due to this, the signals associated with pigments (Fe, As, Ti) are attenuated, and the Ca and S signals are enhanced. The S signal's intensity is still so low that the white paint is more likely to be calcite than gypsum.

The clusters 7 and 8 in Fig. 7c represent areas of restoration, while cluster 10 is the original white paint. Their reflectance spectra are all rather featureless and similar, but they are clearly shown as distinct by the S signal and the presence of Cl in cluster 9. Cluster 7 also features a weak Cu signal, which is due to the limits of lateral resolution discussed above for RIS.

The Cu-containing pigments in the collar are shown in Fig. 7d. While the Cu intensity varies with the layer thickness, no clear difference can be observed in the XRF data. The reflectance spectra are similar to the *endmembers* discussed for RIS in Fig. 4. It is worth noting that the three groups are not clearly separated in the scatter plot in Fig. 6, as the features in the reflectance spectra are of low intensity, so that only little statistical weight was put on them. The cluster for the Egyptian green was mainly found due to *a priori* knowledge from the RIS data alone.

Another observation that can be made is that in all clusters not correlated to later restoration treatments, As was found to be present. This can be due to deliberate or accidental addition of this element, *e.g.*, to a ground or preparation layer, as described for arsenolite (As_2O_3) [18], or if this is due to the migration of As after degradation of orpiment as it has been observed in historical painting [19]. However, the methods employed do not allow us to answer this question.

5. Conclusions

Given the complementary nature of XRF and RIS, their combination allowed us to identify most pigments used in the wall paintings of Nakhtamun's tomb. RIS allowed us to distinct between different Fe-based pigments that had no other characteristic elemental markers. XRF allowed narrowing down the number of pigments potentially involved in a pigment mixture to identify them by RIS.

In practical terms, data acquisition is much faster for RIS and requires no ionizing radiation; but with the wavelength range exploited in this work, the information is limited to surface features. XRF is much slower and can only investigate a fraction of the area investigated by RIS, but its penetrative nature allows also investigating sub-surface layers. However, neither of these techniques allow for the direct identification of chemical species and we intend to complement our measurements in the future with more specific spot analysis techniques, such as XRD or Raman.

For *exploration* and *evaluation* of RIS and XRF data, the established methods were shown to allow an objective evaluation of data. However, *interpretation* and *presentation* are challenged by the fact that two different sets of images need to be compared.

Albeit the selection of the meaningful spectral ranges to be included requires a limited *exploration* of the data, the treatment of fused data by t-SNE is first *evaluated* and then *explored* and *interpreted*. This makes the *representation* more subjective than that of the established methods. One has also to be aware that as an iterative gradient descent method starts from random initial values, the *representations* thus produced are similar but not identical. However, in the work for this paper, no failure of convergence was observed. Finally, a rapid application of this method to large data sets remains limited as computational complexity (O), and with it processing time, for the used Barnes–Hut variant of t-SNE scales with $O(N \log N)$, with N being the number of data points.

Nevertheless, t-SNE with fused data is clearly superior to the established methods in the *presentation* of results. The t-SNE representation clearly highlights the presence of sub-surface layers: the overpainted skin (cluster 9) and the yellow below the red lines (cluster 1), without the need for manual comparison to an aligned photograph, as well as a clear cluster for the dark ink in the yellow area (cluster 5). With improved weighing of the data, it will also be possible to clearly separate Egyptian green (cluster 12) and Egyptian blue (clusters 13–14).

With this representation, it is also straightforward to graphically communicate an insight gained in Egyptian painting technique: the white paint was applied after the contour of the face was finished (Fig. 5 and cluster 9). It was also applied on the yellow paint to limit its extent (cluster 6). After this, the Fe-containing lines were drawn, as they lie on the white and yellow paint (cluster 1). Given the fact that the red paint was so liquid that its color intensifies towards the lower end, as seen in the photographs, this illustrates the mastery of the painters as they dared to paint these final defining lines right above a finished depiction of the deceased, without interfering with it.

Acknowledgements

Appendix A. Supplementary material

Supplementary material related to this article can be found online at https://doi.org/10.1016/j.crhy.2018.08.004.

References

[1] M. Alfeld, J.A.C. Broekaert, Spectrochim. Acta, Part B 88 (2013) 211–230.
[2] M. Alfeld, L. de Viguerie, Spectrochim. Acta, Part B 136 (2017).
[3] J.K. Delaney, K.A. Dooley, R. Radpour, I. Kakoulli, Sci. Rep. 7 (2017) 15509.
[4] M. Alfeld, M. Wahabzada, C. Bauckhage, K. Kersting, G. Wellenreuther, P. Barriobero-Vila, G. Requena, U. Boesenberg, G. Falkenberg, J. Synchrotron Radiat. 23 (2016) 579–589.
[5] E. Pouyet, S. Devine, T. Grafakos, R. Kieckhefer, J. Salvant, L. Smieska, A. Woll, A. Katsaggelos, O. Cossairt, M. Walton, Anal. Chim. Acta 982 (2017) 20–30.
[6] E. Pouyet, N. Rohani, A.K. Katsaggelos, O. Cossairt, M. Walton, Pure Appl. Chem. 90 (2018) 493–506.
[7] B. Porter, R.L.B. Moss, Topographical Bibliography of ancient Egyptian Hieroglyphic Texts, Reliefs, and Paintings, Griffith Institute, Ashmolean Museum, Oxford, UK, 1970.
[8] D.A. Scott, Stud. Conserv. 61 (2016) 185–202.
[9] L. de Viguerie, S. Rochut, M. Alfeld, P. Walter, S. Astier, V. Gontero, F. Boulc'h, Herit. Sci. 6 (2018) 11.
[10] V.A. Solé, E. Papillon, M. Cotte, P. Walter, J. Susini, Spectrochim. Acta, Part B 62 (2007) 63–68.
[11] M. Alfeld, K. Janssens, J. Anal. At. Spectrom. 30 (2015).
[12] C. Cucci, J.K. Delaney, M. Picollo, Acc. Chem. Res. 49 (2016) 2070–2079.
[13] L. van der Maaten, G. Hinton, J. Mach. Learn. Res. 9 (2008) 2579–2605.
[14] S. Colinart, in: W.V. Davies (Ed.), Colour and Painting in Ancient Egypt, British Museum Press, London, 2001.
[15] N. Eastaugh, V. Walsh, T. Chaplin, R. Siddall, The Pigment Compendium, Elsevier, Oxford, UK, 2004.
[16] H. Liang, Appl. Phys. A 106 (2012) 309–323.
[17] B.M. Bryan, in: A.B. Lloyd (Ed.), A Companion to Ancient Egypt, vol. II, Wiley-Blackwell, Oxford, 2010, pp. 1000–1006, and especially 1004;
F. Tiradritti, Painting (materials), in: M.K. Hartwig (Ed.), A Companion to Ancient Egyptian Art, Wiley-Blackwell, Oxford, UK, 2015, pp. 249–268, with bibliography.
[18] S. Pagès-Camagna, E. Laval, D. Vigears, A. Duran, Appl. Phys. A 100 (2010) 671–681.
[19] K. Keune, J. Mass, A. Mehta, J. Church, F. Meirer, Herit. Sci. 4 (2016) 10.